

RESEARCH ARTICLE | AUGUST 15 2024

## Numerical modeling of wave interaction with a porous floating structure consisting of uniform spheres

Special Collection: [Flow and Civil Structures](#)

Yiyong Dong (董毅勇)  ; Weikai Tan (谈伟恺)  ; Hao Chen (陈昊)  ; Jing Yuan (袁兢) 

 Check for updates

*Physics of Fluids* 36, 087133 (2024)

<https://doi.org/10.1063/5.0222161>



### Articles You May Be Interested In

Wave-induced collisions of thin floating disks

*Physics of Fluids* (December 2017)

# Numerical modeling of wave interaction with a porous floating structure consisting of uniform spheres

Cite as: Phys. Fluids **36**, 087133 (2024); doi: [10.1063/5.0222161](https://doi.org/10.1063/5.0222161)

Submitted: 6 June 2024 · Accepted: 26 July 2024 ·

Published Online: 15 August 2024



[View Online](#)



[Export Citation](#)



[CrossMark](#)

Yiyong Dong (董毅勇),<sup>1,2</sup> Weikai Tan (谈伟恺),<sup>3,a)</sup> Hao Chen (陈昊),<sup>4</sup> and Jing Yuan (袁兢),<sup>1,2,a)</sup>

## AFFILIATIONS

<sup>1</sup>Department of Hydraulic Engineering, Tsinghua University, Beijing 100084, China

<sup>2</sup>State Key Laboratory of Hydroscience and Engineering, Tsinghua University, Beijing 100084, China

<sup>3</sup>Department of Port, Waterway and Coastal Engineering, School of Transportation, Southeast University, Nanjing 210096, China

<sup>4</sup>Faculty of Science Agriculture and Engineering, Newcastle University, Newcastle Upon Tyne, NE1 7RU, United Kingdom

**Note:** This paper is part of the special topic, Flow and Civil Structures.

<sup>a)</sup>Authors to whom correspondence should be addressed: [weikai\\_tan@seu.edu.cn](mailto:weikai_tan@seu.edu.cn) and [yuanj2021@mail.tsinghua.edu.cn](mailto:yuanj2021@mail.tsinghua.edu.cn)

## ABSTRACT

Porous materials are increasingly being used in the design of floating structures in coastal and ocean engineering, but there is a lack of numerical tools that can aid in the design of a movable floating porous structure. To close this gap, the existing volume-averaged numerical model for flow interacting with a fixed porous body was extended to floating scenarios by (1) using the relative velocity in the porous friction force, (2) calculating rigid body motion using volume integral of porous body force, and (3) modifying a dynamic mesh algorithm for a mobile porous body. As a demonstration, the developed model was applied to a porous floating structure consisting of cubically packed uniform spheres. Two sets of model applications were involved. The first set considered three-dimensional flow around a fixed porous block placed beneath the free surface. The measured total force on the block under wave or steady flows was predicted accurately with an error less than 10%. The second set involved a two-dimensional wave interacting with a floating porous block representing a breakwater. For free-floating conditions, the model can accurately predict the dynamic response of the structure, including the time varying movement of its rigid body and the mean drift. For mooring-restrained conditions, the mooring force and wave transmission coefficients were also predicted well with an error less than 20%. The proposed numerical approach can be applied to other floating structures with a rigid volumetric porous body. Future research is also required to study the microscopic pore flows, upon which more detailed parameterization of the porous media can be derived.

© 2024 Author(s). All article content, except where otherwise noted, is licensed under a Creative Commons Attribution (CC BY) license (<https://creativecommons.org/licenses/by/4.0/>). <https://doi.org/10.1063/5.0222161>

19 November 2024 06:05:45

## I. INTRODUCTION

Many coastal structures can be conceptualized as porous media, e.g., rubble-mound breakwater (Sollitt and Cross, 1972; Losada *et al.*, 2008), perforated seawalls (Feichtner *et al.*, 2021), fishing net cages (Chen and Christensen, 2016; 2017), flexible porous membranes (Koley *et al.*, 2022; Guo *et al.*, 2020b), suspended canopy (Jie, 2020), granular-material seabed (Rose, 1945), etc. When coastal flow driven by waves and/or current passes through such structures, the flow's mechanical energy can be heavily dissipated by the frictional processes within the pores, which motivates coastal engineers to use porous media for coastal protection (Dong *et al.*, 2008; Wang and Sun, 2010; and Shih, 2012) or reducing wave loads (He *et al.*, 2012; Ji *et al.*, 2016; and Zhang *et al.*, 2023). Designing porous coastal structures requires a

good understanding of the underlying hydrodynamic processes and simple-yet-realistic modeling capabilities, which have been intensively studied over the past decades [see the reviews by Chwang and Chan (1998); Guo *et al.* (2020a); and Han and Wang (2022)].

For many engineering applications, the bulk behavior of porous media flow is the primary interest, such as wave dissipation of rubble-mound breakwater and bulk velocity of groundwater flow, so the presence of porous media is often conceptualized as adding a body force to the flow, and the porous structure becomes a "sponge" zone in either theoretical models or computational-fluid-dynamics (CFD) models. Consequently, the research focus is developing various closure models, which includes empirical parameters that represent the characteristics of porous zones. Based on his experimental work, Darcy (1856)

proposed that the hydraulic gradient (the friction force per unit volume due to porous media) for the flow passing a sand filter column varies linearly with the flow velocity. Rose (1945) conducted experiments with fluid flow passing a bed of granular material and found that Darcy's law fails when the flow velocity becomes sufficiently large. Forcheimer (1901), followed by Dagan (2012), added a quadratic term of velocity to Darcy's formula and extended its applicability to high Reynolds number flows. For unsteady flow, Polubarnova-Kochina (1952) further added the inertia force, so the porous body force  $f_s$  is

$$f_s \propto au + b|u|u + c \frac{\partial u}{\partial t}, \quad (1)$$

where  $u$  is the bulk velocity,  $t$  is time, and  $a$ ,  $b$ , and  $c$  are dimensional empirical coefficients related to both porous material and flow conditions. For modeling groundwater flow through sand, Engelund (1953) proposed the empirical formulas for  $a$  and  $b$ , viz.,

$$a = \alpha \frac{(1 - \phi)^3}{\phi^2} \frac{\nu}{gD_{50}^2}, \quad b = \beta \frac{1 - \phi}{\phi^3} \frac{1}{gD_{50}}, \quad (2)$$

where  $\phi$  and  $D_{50}$  are the porosity and mean nominal diameter of sand, respectively,  $\nu$  is fluid kinematic viscosity,  $g$  is the gravity acceleration, and  $\alpha$  and  $\beta$  are two empirical coefficients. Van Gent (1992) and Gu and Wang (1991) proposed the same formulas for  $c$ ,

$$c = \left[ 1 + \frac{\gamma(1 - \phi)}{\phi} \right] / \phi g, \quad (3)$$

where  $\gamma$  is an also empirical coefficient, and usually taken as 0.34.

Many researchers in the coastal engineering community applied this macroscopic approach in numerical simulation of rubble-mound breakwater. Sollitt and Cross (1972) added Eq. (1) as an extra body resistance force in the momentum equation for fluids and ignored the viscous force. Through linearization of the problem, their analytical solution shows a good performance in terms of calculating reflection and transmission coefficients of rubble-mound breakwaters. Subsequently, Van Gent (1996) and Troch and De Rouck (1998) proposed two-dimensional vertical (2DV) CFD models for rubble-mound breakwater based on Reynolds-averaged Navier-Stokes (RANS) equations, which has been successfully applied in many practical engineering problems. Liu *et al.* (1999), followed by Hsu *et al.* (2002), rigorously introduced the porous media's effects in RANS simulation through carefully volume-averaging the equations, and the porous effect was incorporated in turbulence closure models. This volume-averaged RANS (called VARANS hereafter) model has been extensively applied for CFD simulations of rubble-mound breakwaters [e.g., Lara *et al.* (2008); Losada *et al.* (2008)]. More recently, with the rapid growth of computational resources, del Jesus *et al.* (2012) and Higuera *et al.* (2014a; 2014b) further extended the VARANS model to three-dimensional CFD simulation.

In the above-mentioned CFD studies, little attention is paid to porous floating structures, which is an emerging research area in coastal engineering. The most representative application is perhaps the porous floating breakwater, which relies on flow energy dissipation within the pores to attenuate incoming water waves. The concept has been proposed for decades [e.g., Sollitt and Cross (1972)], but the technology readiness has yet reached the level for widespread commercial application. Most previous studies focused on the design of porous

elements, e.g., diamond-shaped blocks (Wang and Sun, 2010), perforated membranes (Koley *et al.*, 2022; Guo *et al.*, 2020b) and sponges (Zhang *et al.*, 2023). Some researchers added a porous structure onto existing floating breakwater to enhance wave reduction [e.g., Christensen *et al.* (2018)]. These studies were mainly based on laboratory experiments, and they collectively showed that making the floating body porous can indeed enhance wave attenuation and reduce the structure's 6-degree-of-freedom (6DoF) response and hence the mooring force. However, research on the numerical simulation of floating porous structures remains limited. Comparing to modeling wave interaction with a fixed porous structure, which mainly focuses on predicting the time-averaged phenomenon (such as wave attenuation), modeling a floating porous structure also requires a precise prediction of intra-wave flow forces, which is needed for calculating the structure's dynamic response. Certain modifications are required to extend the existing numerical models for fixed porous structures to moving porous structures. For instance, the calculation of porous body force should use the relative velocity,  $u_{rd}$ , between solid and fluid, i.e., replacing  $u$  in Eq. (1) with  $u_{rd}$ . Chen and Christensen (2017) followed this approach and developed an OpenFOAM solver for modeling flexible fish net cage in coastal flows, but this type of structure is not a volumetric porous body. Overall speaking, whether CFD can model the dynamics of floating porous coastal structure is an open question, which motivates this study.

The aim of this paper is to develop a CFD approach for modeling floating porous structures that can be conceptualized as a rigid volumetric porous zone. This is achieved through coupling a VARANS solver, a rigid-body 6DoF solver, and a mooring system solver. The VARANS and 6DoF solvers are modified to account for a moving porous body. As a demonstration, we applied the developed model to simulate wave interaction with a porous floating structure consisting of uniform spheres [see Fig. 1(a) for a conceptual sketch] and conducted some laboratory experiments to obtain the necessary data for model validation. The outline of this paper is as follows: Section II introduces the governing equations of the proposed numerical simulation and the numerical implementation. Section III introduces a simple volumetric porous structure consisting of cubically packed uniform spheres and the setup of flume experiments. Sections IV and V present model validation for 3D flow around a fixed porous structure and 2D wave-structure interaction. Finally, conclusions are drawn in Sec. VI.

## II. INTRODUCTION OF THE PROPOSED NUMERICAL APPROACH

In this section, the proposed numerical approach for modeling a floating porous structure is presented. Our work is based on the OpenFOAM solver for coastal engineering problems involving porous media, i.e., the IHFOAM solver developed by Higuera *et al.* (2014a). Modifications of the theory and codes are presented here for future references.

### A. Extension of the VARANS solver for floating porous structures

A brief introduction of VARANS for simulating porous media flow is first provided here. The volume,  $V$ , of porous media consists of a solid part (with volume,  $V_s$ , and velocity,  $u_s$ ) and a fluid part (with volume,  $V_f$ , and velocity  $u$ ), as shown in Figs. 1(b) and 1(c).

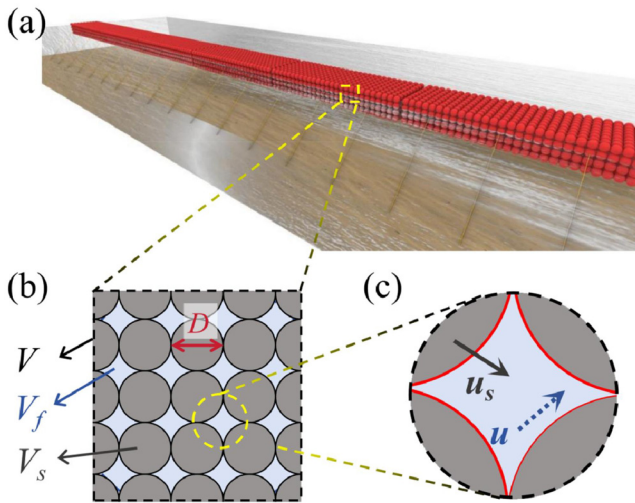


**FIG. 1.** A sketch of the porous floating structure consisting of sphere units: (a) design of porous floating structure, (b) control volume, and (c) control volume (details).

The volume average ( $\langle \rangle$ ) and intrinsic volume average ( $\langle \rangle^f$ ) of variables within a porous media are defined as follows:

$$\langle \xi \rangle = \frac{1}{V} \int_{V_f} \xi dV, \quad \langle \xi \rangle^f = \frac{1}{V_f} \int_{V_f} \xi dV. \quad (4)$$

Here,  $\xi$  is any field variable inside porous media, which can be subsequently written as follows:

$$\xi = \langle \xi \rangle + \xi'', \quad (5)$$

where  $\xi''$  denotes the spatial fluctuations. For engineering applications, the volume-averaged quantities are of the primary interest. Liu *et al.* (1999), followed by Higuera (2015), applied volume averaging to RANS equations. Similar to the Reynolds stress given by the correlation between the turbulent fluctuations of velocity components, the correlation between spatial fluctuations of velocity components gives a stress governing the behavior of volume-averaged flow, which is treated as a volumetric resistance force in the momentum equation of VARANS. The readers may refer to Higuera (2015) for more details of the derivation. Eventually, the VARANS equations for coastal-engineering problems involving free water surface are

$$\nabla \cdot \langle \mathbf{u} \rangle = 0, \quad (6)$$

$$\begin{aligned} \frac{1+C\partial\rho\langle\mathbf{u}\rangle}{\phi} + \frac{1}{\phi} \nabla \cdot \left( \frac{\rho\langle\mathbf{u}\rangle\langle\mathbf{u}\rangle}{\phi} \right) \\ = -\nabla\langle p \rangle^f + \rho\mathbf{g} + \nabla \cdot \mu_{eff} \nabla \left( \frac{\langle \mathbf{u} \rangle}{\phi} \right) - \mathbf{F}_d, \end{aligned} \quad (7)$$

$$\frac{\partial\alpha}{\partial t} + \frac{1}{\phi} \nabla \cdot (\alpha\langle \mathbf{u} \rangle) + \frac{1}{\phi} \nabla \cdot [\alpha(1-\alpha)\langle \mathbf{u}_{ra} \rangle] = 0, \quad (8)$$

where  $\mathbf{F}_d$  is the porous friction force per unit volume,  $\rho$  is the fluid density,  $p$  is the pressure, and  $\mathbf{g}$  is the gravity acceleration.  $\mu_{eff}$  is the effective viscosity defined as  $\mu_{eff} = \mu + \mu_T$ , where  $\mu$  is the dynamic viscosity and  $\mu_T$  is the turbulence eddy viscosity.  $\alpha$  ( $0 \leq \alpha \leq 1$ ) is the

volume fraction of fluid, and  $\mathbf{u}_{ra}$  is the relative velocity between fluid and air. We included the  $k-\epsilon$  turbulence closure model for describing  $\mu_T$  in our simulation. We utilized the volume of fluid (VOF) method (Hirt and Nichols, 1981) for simulating multi-phase flow to model the interaction between liquid and gas. The core idea of the VOF method is to track the position of the fluid interface rather than modeling it as a fixed interface. This is achieved by monitoring the variations in the fluid volume fraction to capture the movement of the fluid interface. The properties of the fluid in each cell can be calculated by weighting them with the  $\alpha$ . To illustrate, the density of the fluid in Eq. (7) can be calculated as follows:

$$\rho = \alpha \rho_{water} + (1 - \alpha) \rho_{air}, \quad (9)$$

where  $\rho_{water}$  is the water density and  $\rho_{air}$  is the air density. The transport equation [Eq. (8)] of  $\alpha$  is solved with the multidimensional universal limiter for explicit solution (MULES) (Rusche, 2002).

To consider a moving porous body,  $\mathbf{F}_d$  is determined following the Darcy–Forchheimer equation but with the relative velocity  $\mathbf{u}_{rd}$ , viz.,

$$\mathbf{F}_d = A \langle \mathbf{u}_{rd} \rangle + B |\langle \mathbf{u}_{rd} \rangle| \langle \mathbf{u}_{rd} \rangle. \quad (10)$$

The inertial force is calculated using the local fluid velocity  $\mathbf{u}$  instead of the relative velocity  $\mathbf{u}_{rd}$  for simplicity. For the application (porous floating breakwater) in this study, the inertial force is much smaller than the porous friction force, and it does not contribute to flow energy dissipation, so this simplification does not affect model performance. In fact, there is little knowledge of added-mass coefficient [C in Eq. (7)], for a moving porous medium in wave-induced flows, which “forces” us to assume that the acceleration of the solid body is much smaller than the fluid’s acceleration, and still use  $\mathbf{u}$  to calculate the inertial force. This assumption is acceptable for heavy floating structures with rather rigid mooring, but may not be valid for small structure or flexible mooring (such as catenary-line mooring with a long chain laid on the seabed). Future research is needed to illustrate the mechanism and modeling of inertial force for moving solid body in wave flows.

Without loss of generality, the coefficients for  $\mathbf{F}_d$  can be written as follows:

$$A = \begin{bmatrix} A_x & 0 & 0 \\ 0 & A_y & 0 \\ 0 & 0 & A_z \end{bmatrix}, \quad B = \begin{bmatrix} B_x & 0 & 0 \\ 0 & B_y & 0 \\ 0 & 0 & B_z \end{bmatrix}, \quad (11)$$

where  $xyz$  is the Cartesian coordinate, representing streamwise, spanwise, and vertical directions in this study. When the diagonal components are the same, the porous media is considered isotropic. Anisotropy may come from the anisotropy of the geometry of the porous structure (e.g., one direction has less openings than the other direction) or complex flow-structure interaction. This study is aimed at demonstrating the proposed numerical approach, so we shall only consider isotropic problems for simplicity. The coefficient matrices become scalars and are calculated as follows (Van Gent, 1996):

$$A = \alpha \frac{(1-\phi)^2}{\phi^3} \frac{\mu}{D^2}, \quad (12)$$

$$B = \beta \frac{1-\phi}{\phi^3} \frac{\rho}{D}. \quad (13)$$

$$\beta = \beta_c \left( 1 + \frac{7.5}{KC} \right), \quad (14)$$

$$C = \frac{\gamma(1-\phi)}{\phi}. \quad (15)$$

Here,  $D$  is the equivalent diameter of the element of porous body, and  $\alpha$ ,  $\beta$ , and  $\gamma$  are dimensionless coefficients, which mainly depend on the geometric characteristics of the pores for high Reynolds number. In addition, the parameter  $\beta$  is divided into two components: the stationary flow contribution  $\beta_c$  and an additional resistance in the case of an oscillatory wave motion, and this additional resistance is shown as function of the Keulegan–Carpenter number ( $KC$ ).

## B. Modification of the 6DoF solver for a rigid-body porous floating structure

In the present study, we focus on the rigid-body porous structures. Therefore, the response of the porous structure is reduced to 6DoF motion response. For typical floating structures, the external loadings are flow loadings, gravity and mooring loadings. In CFD modeling of large voidless floating structures, flow loadings are calculated by integrating pressure and shear forces over the external surface, which is not applicable for porous structures. Following the treatment of porous force in VARANS, the flow loading is considered as a body force,  $f_s$ , distributed over the entire porous body, so the total flow loading for 6DoF calculation is given by integrating  $f_s$  over the volume of the porous media. Hence, the 6DoF of floating porous structures are simulated through the following equations:

$$M \frac{d\mathbf{u}_s}{dt} = \iiint_V f_s dV + \mathbf{F}_{mooring} + \mathbf{G}_s \quad (16)$$

and

$$I \frac{d\omega_s}{dt} = \iiint_V \mathbf{r}_{CS} \times f_s dV + \mathbf{r}_{CM} \times \mathbf{F}_{mooring} - \omega_s \times (\mathbf{I} \cdot \omega_s) + \mathbf{r}_{CG} \times \mathbf{G}_s, \quad (17)$$

where  $M$  is the total mass of porous floating structure,  $\mathbf{I}$  denotes the moment of inertia,  $\mathbf{u}_s = (u_{s,1}, u_{s,2}, u_{s,3})$  and  $\omega_s = (\omega_1, \omega_2, \omega_3)$  are the linear and angular velocities of the porous body, respectively,  $\mathbf{r}_{CS}$ ,  $\mathbf{r}_{CM}$  and  $\mathbf{r}_{CG}$  are the momentum arms for  $f_s$ , mooring forces and gravity, respectively,  $\mathbf{G}_s$  is gravity, and  $\mathbf{F}_{mooring}$  is the fairlead mooring forces.

The body force on the porous media,  $f_s$ , includes three parts: the friction force  $f_d$ , the inertial force  $f_i$ , and the pressure force  $f_p$ . Note that the friction force  $f_d$  has included the pressure force due to spatially varying pressure within the pores [see Higuera *et al.* (2014a)], so  $f_p$

here covers the pressure force from the intrinsic volume-average pressure. The expression for  $f_s$  is

$$f_s = f_d + f_i + f_p \\ = A \langle \mathbf{u}_{rd} \rangle + B |\langle \mathbf{u}_{rd} \rangle| \langle \mathbf{u}_{rd} \rangle + \frac{C}{\phi} \frac{\partial \rho \langle \mathbf{u} \rangle}{\partial t} - (1-\phi) \nabla \langle p \rangle^f. \quad (18)$$

Under hydrostatic condition, volume integrating  $f_p$  over the underwater part of the porous body gives the buoyancy force for a porous floating body.

## C. Modification of dynamic mesh for a rigid-body porous floating structure

The original dynamic mesh in OpenFOAM only applies to a rigid body, since the inner boundary of the mesh deformation region is defined as a certain distance from the body's solid boundary, whereas the porous zone does not have a solid boundary. Therefore, the way to define a region with mesh deformation is modified to account for the movement of a porous body. As shown in Fig. 2(a), we define two concentric ellipsoids enclosing the porous body. The mesh within the inner ellipsoid is defined as the inner zone, which follows the movement of the porous body and remains unchanged. The mesh outside the outer ellipsoid is defined as the outer zone, which remains static. The mesh between the two is defined as the deformation zone, which is stretched/compressed to allow the movement of the entire inner zone [Fig. 2(b)]. The size of inner ellipsoid is based on the size of the porous body, whereas the size of the outer ellipsoid depends on the expected displacement of the body over the entire simulation.

## D. The model for a mooring system

In state-of-the-art numerical simulations of moored floating structures, dynamic mooring models, based on the lumped-mass method [e.g., MoorDyn proposed by Hall (2015)] or finite-element method [e.g., Moody proposed by Palm *et al.* (2017) and Palm (2017)], have been coupled with CFD codes for high-fidelity modeling of wave-structure interactions. In the present study, the model application is porous floating porous structure with a taut mooring, so the Moody model, which is more suitable for such applications, is selected and briefly introduced here.

Moody solves for the motion of an unstretched cable based on the assumption of negligible bending stiffness. The calculation of the cable's position is governed by the following equation:

$$\frac{\partial^2 \mathbf{r}_m}{\partial t^2} = \frac{1}{\gamma_0} \frac{\partial T}{\partial s} + \frac{\mathbf{f}}{\gamma_0}, \quad (19)$$

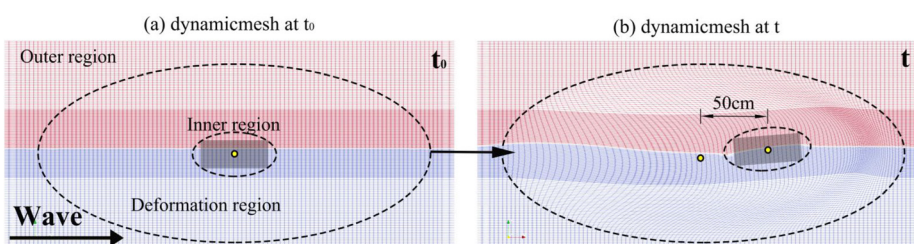


**FIG. 2.** 2D computational dynamic mesh for wave attacking a free-floating porous structure (red region: air, blue region: water): (a) dynamic mesh at  $t_0$  and (b) dynamic mesh at  $t$ .

where  $\mathbf{r}_m$  is the cable position vector in a curvilinear coordinate ( $s$ ) of the unstretched cable domain,  $\mathbf{t}$  is the unit tangential vector,  $\gamma_0$  denotes the cable mass per meter, and  $\mathbf{f}$  represents external forces including added mass, Froude-Krylov force, drag force, gravity, buoyancy, and contact forces due to the interaction with seabed.  $T$  is the axial tension force, which is calculated via

$$T = \|\mathbf{T}\| \frac{\mathbf{q}}{1 + \epsilon}, \quad (20)$$

where  $\epsilon$  is the axial strain and  $\mathbf{q}$  is an auxiliary variable related to the axial strain of cables, i.e.,  $\mathbf{q} = \frac{\partial r}{\partial s} \|\mathbf{T}\|$  denotes the magnitude of tension, which can be linearized as  $\|\mathbf{T}\| = EA_0\epsilon$  for simplicity, where  $EA_0$  is the axial stiffness.

The above governing equations are solved through a high-order finite element method. An hp-adaptive discontinuous Galerkin method is adopted for snap loads, which makes it suitable for the taut mooring system used in this study.

## E. Numerical implementation

The present numerical approach is implemented by modifying the IHFOAM solver in OpenFOAM (v2206). Following the introductions in Secs. II A–II C, the changes to the IHFOAM source codes are as follows. First, in the momentum equation, the friction force due to porous media [i.e., Eq. (10)] is calculated using the relative velocity  $\mathbf{u}_{rd}$  instead of fluid velocity  $\mathbf{u}$ . Second, the original 6DoF solver for calculating rigid body motion in OpenFOAM is revised. The body force at

each cell center of the porous zone is evaluated using Eq. (18), and subsequently used to calculate 6DoF according to Eq. (16). Third, we adopted the code of Chen and Hall (2022) to couple the mooring model, Moody [e.g., Palm *et al.* (2016)], with the OpenFOAM solver.

To better visualize the process of the proposed numerical simulation, a flow chart is provided in Fig. 3. The outer loop is mainly for IHFOAM to model hydrodynamics. The 6DoF module contains the calculation of forces and moments due to porous structure, which are then needed to calculate the motion of porous structure. The motion status is passed to the mooring module, such that the tension at fairlead is returned to the 6DoF module. Iterations are required for this coupling process. It is noteworthy that the dynamic mesh function provided by OpenFOAM is adopted to account for rigid body motion.

## III. EXPERIMENTAL SETUP

### A. Introduction of porous structures consisting of uniform spheres

In the present study, an example of porous media, i.e., cubically packed uniform spheres [Fig. 1(a)], is selected for demonstrating the proposed numerical approach. The projections of the structure's pores in streamwise  $x$ , spanwise  $y$ , and vertical  $z$  directions appear identical, so the porous media is believed to be isotropic. As discussed in Sec. II, there are three empirical coefficients  $\alpha$ ,  $\beta$ , and  $\gamma$  in the body force model representing the porous media effect.

Van Gent (1996) has studied these parameters for various porous structures using an oscillatory water tunnel, in which the total force was estimated using measurements of pressure drop of one-

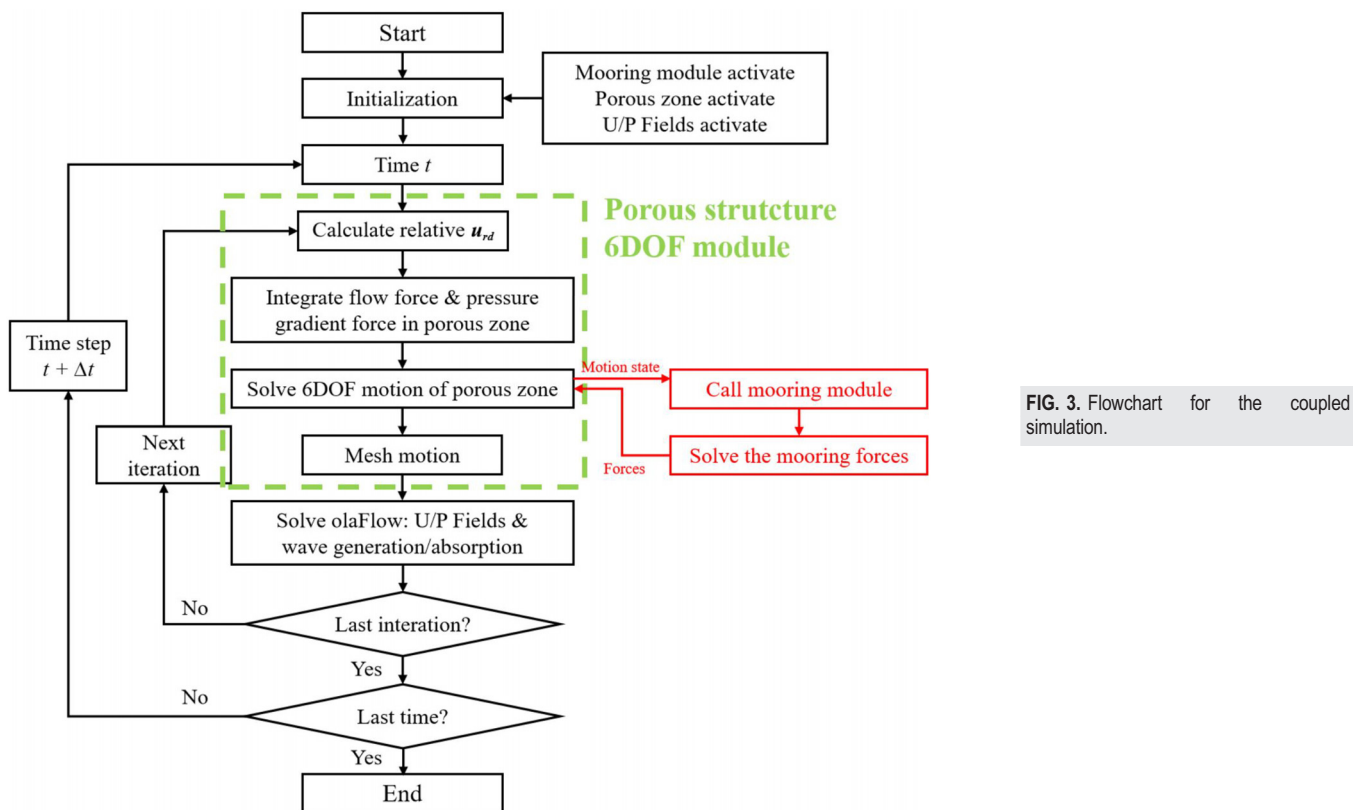
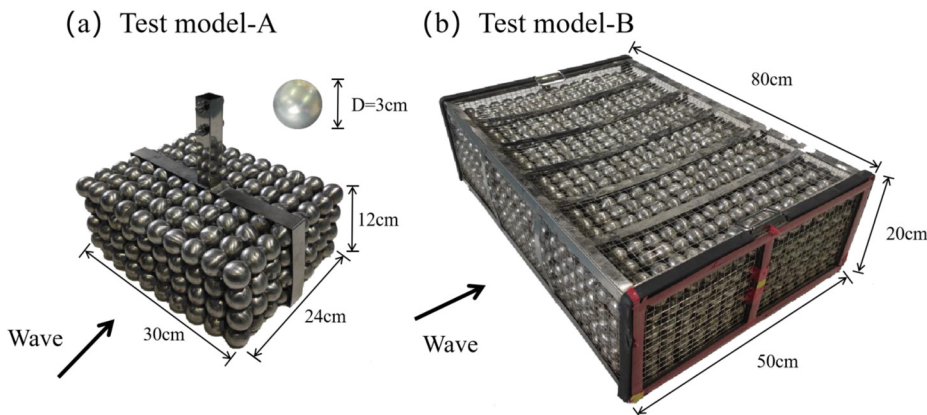


FIG. 3. Flowchart for the coupled simulation.



**FIG. 4.** An overview of the test model: (a) test model-A and (b) test model-B.

dimensional flow through the porous media. One of his test models was cubically packed spheres with  $D = 4.6$  cm. He found that  $\alpha$  is 1500 and  $\beta$  is 0.69 for current flows.  $\alpha$  is 2070 and  $\beta$  is 0.55 ~ 1.2 for oscillatory (wave) flows under  $KC = 6 \sim 93$ , and  $\beta$  reduces as  $KC$  increases, which can be described by Eq. (14). Note that Eq. (14) is mainly calibrated for  $KC > 10$ , while for lower  $KC$  values, Smith (1991) found that  $\beta$  has little variation. For the simulations presented in this paper,  $KC$  is mostly less than ten, so we simply ignore the variation of  $\beta$  with  $KC$  and take  $\beta = 1.2$ , which is the upper bound of  $\beta$  from the oscillatory-flow test with  $KC = 6$  of Van Gent (1996). This simplification also bypasses the issue that at certain place the flow velocity may be zero, which leads to  $KC = 0$  and hence infinite  $\beta$  according to Eq. (14). In addition, Van Gent (1996) also found that the linear term  $A\mathbf{u}$  is much smaller than the quadratic term  $B|\mathbf{u}|\mathbf{u}$ , so we simply adopted  $\alpha = 2070$  from his oscillatory flow tests.

In this study, the porous structures have a rectangular cross-section and consist of cubically packed uniform hollow spheres ( $D = 3.2$  cm and bulk density  $\rho_B = 680$  kg/m<sup>3</sup>). As shown in Fig. 4, the first model (model-A) is smaller and has a size of 24 cm (length) × 30 cm (width) × 12 cm (height). Its width is 3/8 of the width of the flume, so the flow around it is three-dimensional. The second model (model-B) has a size of 50 cm (length) × 80 cm (width) × 22 cm (height), which has the same width as the flume, so its interaction with incoming wave in the flume can be considered as a two-dimensional problem. It is placed inside a metal frame to ensure the integrity of the overall structure. Parameters of two models are shown in Table I.

Model-B is placed within a containing frame. The weight of the frame is 1.2 kg, which is only 5% of the total weight of model-B. This additional mass is included in the bulk parameter of the spheres. The meshes on the six sides of the frame are made of metal wires (diameter 0.8 mm), and have a grid size of 13 mm. These meshes are similar to fish nets, so we used the drag parameters proposed by Chen and Christensen (2016) to evaluate their contribution to total drag force. It is found that under the test conditions in this study the drag on the meshes is less than 2% of the drag on the spheres. Therefore, the influence of the containing frame is negligible.

## B. Setup of flume experiments

Experiments were conducted in a wave flume at the hydraulic lab in Tsinghua University. A sketch of the facility is provided in Fig. 5.

The flume body is 20 m in length, 0.8 m in width, 0.8 m in depth. A piston-type wave generator is mounted at one end of the flume, which is able to generate wave height,  $H$ , between 0.03 and 0.05 m, wave period  $T$ , between 0.5 and 2.0 s. A towing system is built above the flume, of which the towing distance is up to 10 m, and the maximum towing speed is 2 m/s.

### 1. Tests with fixed porous structure suspended in water

The experiments using model-A were designed to validate prediction of total body force on the porous structure in unsteady or steady flows. Therefore, model-A was mounted to a force sensor, which was then mounted to the towing carriage above the flume, as shown in Fig. 6(b). The upper surface of model-A was aligned with the still water surface in each test, so the block was initially fully submerged. The force sensor is ZNHM-D-50 kg from CHINO SENSOR company, and it offers continuous three-dimensional force measurements with a frequency of 50 Hz and an accuracy of 1.5 N. The block is suspended in water, and the instantaneous streamwise ( $x$  direction) and vertical ( $z$  direction) total flow forces were measured by the force sensor. Two types of flow conditions were involved, i.e., towing tests and wave tests.

**TABLE I.** Key parameters of test model.

	Value	Unit
Test model-A		
Size (streamwise × spanwise × vertical)	24 × 30 × 12	cm
Porosity	0.45	...
Density (solid portion)	0.68	...
Weight	3.2	kg
Sphere diameter ( $D$ )	3.2	cm
Test model-B		
Size (streamwise × spanwise × vertical)	50 × 80 × 20	cm
Porosity	0.45	...
Density (solid portion)	0.68	...
Weight	29.9	kg
Sphere diameter ( $D$ )	3.2	cm

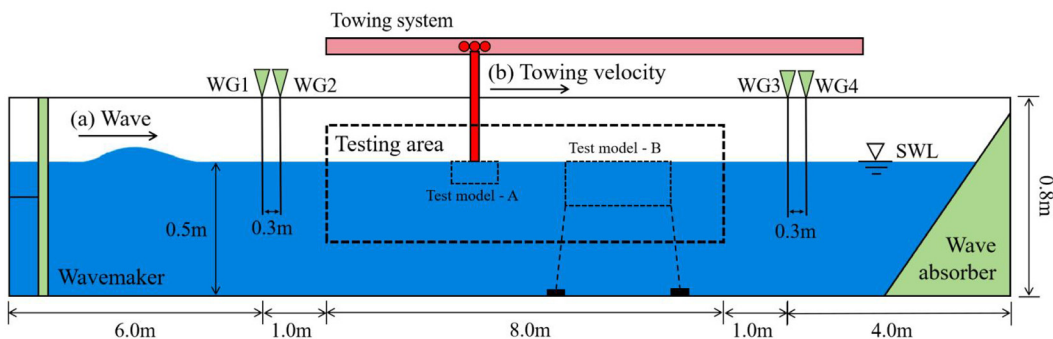


**FIG. 5.** An overview of the experimental setup. Wave is generated from the left side of the flume. The fixed porous structure (model-A) is fixed on towing system, which can be towed at a constant speed. The floating porous structure (model-B) is connected with four steel chains and anchor weights.

In towing tests (steady-flow conditions), the model block was towed at a constant speed, and the inline force was measured. In wave tests (unsteady-flow conditions), the model block did not move, and the periodic wave loading on the block was measured.

## 2. Tests with floating porous structures

The experiments using model-B is to mimic a classic problem of coastal engineering, i.e., wave attenuation by a porous floating breakwater. For breakwater studies, it is conventional to first study two-dimensional problem, i.e., normally-incident long-crest waves hit the breakwater. We conducted free-floating experiments and mooring-restrained experiments. As shown in Fig. 5, the model-B was placed at 12 m from the flume's wave maker. In mooring-restrained experiments, the model-B was just fully submerged, i.e., the top of the model was at the still water surface. The mooring system consists of four 0.43 m-long steel chains connecting the four bottom corners of the

model-B to anchoring weights placed on the flume bottom (Fig. 7). We only consider taut mooring in this paper, so during the tests the mooring lines were fully taut, and were at a 5° angle to the z direction. Parameters of mooring are summarized in Table II.

Two pairs of wave gauges were placed on both sides of the model for quantifying incident, reflected and transmitted periodic waves using the method proposed by Mansard and Funke (1980). To measure the 3DoF (i.e., translations in x and z directions and rotation around the y axis), two markers, one at the center of gravity (CoG) and one at the bottom-left corner, were placed on the model, and a stream camera (1080 P, 60 fps) was used to obtain video recordings, from which, the displacements of the two markers were manually read. The accuracy of determining the locations of marker is 0.5–1 pixel, which is equivalent to 0.4–0.7 mm. A one-dimensional tension sensor (ZNLBS – 100 kg) was inserted in each mooring chain, which offers measurement of tension force with a sampling rate of 50 Hz and an accuracy of 3 N. Since all sensors were wired to the same

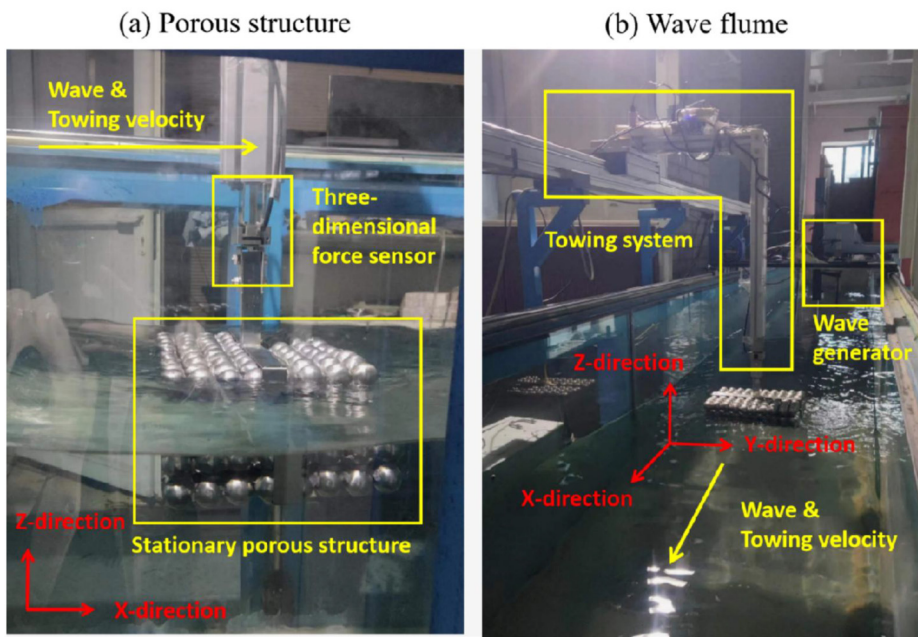


**FIG. 6.** The setup of tests using fixed porous body (model-A): (a) the placement of the model in the flume and (b) overall test setup.

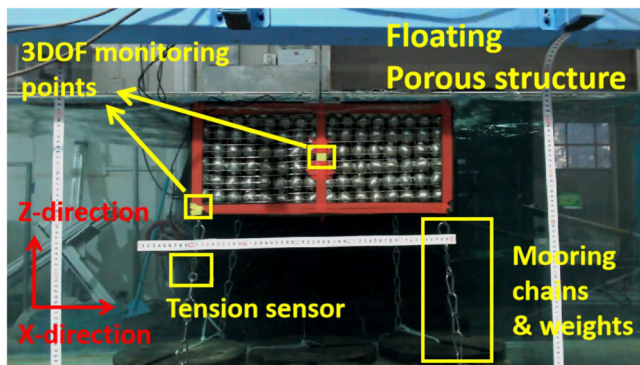


FIG. 7. Experimental setup of a porous structure with taut mooring (model-B).

data logger, the measurements of water level, mooring force and video were automatically synchronized.

### C. Test conditions

Test conditions for model-A are given in Table III. In towing tests, the porous structure was towed with 10 different velocities (from 0.1 to 1.0 m/s). In wave tests, periodic waves were generated with the same wave period  $T = 1.2$  s, but varying wave height,  $H_i$ . The water depth  $h$  was 50 cm for all tests, and the top of the model was aligned with the still water surface. All tests were repeated twice to check the repeatability.

Totally seven tests with model-B were involved in this paper, which are summarized in Table IV. All tests have periodic waves with the same wave height,  $H_i = 5.7$  cm but varying wave period,  $T$ . There was a slight difference of  $H_b$  due to the imperfect wave generation, and we have used the two upstream wave gauges to accurately measure the incident  $H_i$  among the tests. The water depth  $h$  was 64 cm, which made the test model-B just fully submerged when connected to the mooring system in mooring-restrained experiments, i.e., the top of the model was at the still water surface. The wave speed is 1.5–2.0 m/s under the given wave period and wave depth.

As shown in Fig. 5, the distance between two upstream wave gauges and porous structure is about 6 m, and the distance between two upstream wave gauges is 30 cm. A key parameter for wave-induced response of floating porous structure is the ratio  $B/L$ , where  $B$  is porous structure's width and  $L$  is wavelength. We selected  $T$  between 0.9 and 1.4 s, so  $B/L$  is between 0.18 and 0.40. All tests were repeated three times for checking the experimental error.

TABLE II. Key parameters of mooring.

	Value	Unit
Length	$43 \times 4$	cm
Equivalent diameter	1	cm
Mass/length	6	g/cm <sup>3</sup>
Angle to the z direction	5	°
Anchoring weights (upstream)	$40 \times 2$	kg
Anchoring weights (downstream)	$20 \times 2$	kg

TABLE III. Test conditions for 3D fixed tests ( $T_{t1}$  to  $T_{t10}$  are towing tests,  $T_{w1}$  to  $T_{w6}$  are wave tests).

Test ID	Wave height $H_i$ (cm)	Wave period $T$ (s)	Towing velocity $U_t$ (m/s)	Repeats
$T_{t1}$	...	...	0.1	2
$T_{t2}$	...	...	0.2	2
$T_{t3}$	...	...	0.3	2
$T_{t4}$	...	...	0.4	2
$T_{t5}$	...	...	0.5	2
$T_{t6}$	...	...	0.6	2
$T_{t7}$	...	...	0.7	2
$T_{t8}$	...	...	0.8	2
$T_{t9}$	...	...	0.9	2
$T_{t10}$	...	...	1.0	2
$T_{w1}$	3.3	1.2	...	2
$T_{w2}$	4.1	1.2	...	2
$T_{w3}$	4.8	1.2	...	2
$T_{w4}$	5.8	1.2	...	2
$T_{w5}$	7.7	1.2	...	2
$T_{w6}$	8.7	1.2	...	2

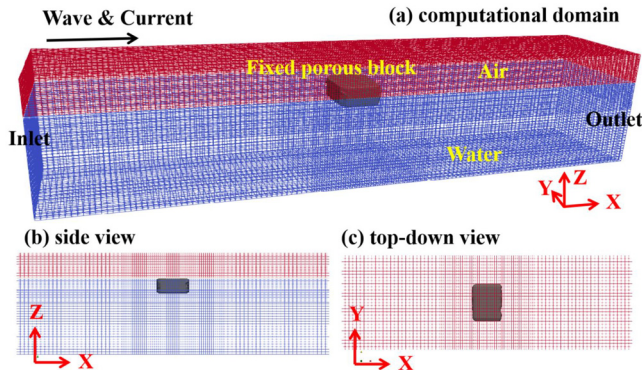
## IV. MODEL APPLICATION: FIXED POROUS STRUCTURE

### A. Setup of numerical simulation

The proposed numerical model was applied to fixed porous structures in towing and waves tests to validate the prediction of total body force. Since the width of the porous block is smaller than that of the flume, a 3D computational domain is constructed as in Fig. 8. The streamwise length of the domain is 4 m long, which covers about two wave lengths of the wave tests. The width of the domain is the same as the flume width. The depth of the domain is 80 cm, of which the bottom 50 cm is water and the top 30 cm is air. Since it is difficult to realize towing in numerical model, towing tests are treated as “current” tests in our simulations, i.e., the porous block does not move in the simulation, and an incoming current with a speed matching the towing speed is generated toward the block. Inflow and outflow boundary conditions are specified using the IHFOAM toolbox. No-slip boundary conditions are applied at the two sides, top and bottom. A structured

TABLE IV. Test conditions for 2D floating tests ( $T_f$  is a free floating test,  $T_{m1}$  to  $T_{m6}$  are moor-restrained tests).

Test ID	Wave height $H_i$ (cm)	Wave period $T$ (s)	Wave length $L$ (m)	$B/L$	Mooring	Repeats
$T_f$	5.6	1.2	2.17	0.23	...	3
$T_{m1}$	5.4	0.9	1.25	0.40	taut	3
$T_{m2}$	5.8	1.0	1.51	0.33	taut	3
$T_{m3}$	5.5	1.1	1.85	0.27	taut	3
$T_{m4}$	5.7	1.2	2.17	0.23	taut	3
$T_{m5}$	5.5	1.3	2.50	0.20	taut	3
$T_{m6}$	6.0	1.4	2.78	0.18	taut	3



mesh was used in the simulation with details shown in Figs. 8(b) and 8(c). To capture the deformation of the free surface, the mesh is first refined in the  $\pm 15$  cm region on both sides of the free surface, which is sufficient to accommodate the surface waves in wave tests. For better capturing the volumetric porous force, the mesh is also refined within the porous zone. The total amount of grids is  $2.7 \times 10^5$ . The time step was set 0.01 s and will be adjusted according to the Courant number. The total simulation time was 30–50 s. Convergence tests have been

performed in A to confirm that this grid resolution is sufficiently fine. The  $x$  and  $z$  components of total porous force experienced by the model block are defined as follows:

$$\mathbf{F}_s = (F_x, F_y, F_z) = \iiint_V f_s dV. \quad (21)$$

## B. Towing tests

The six towing tests ( $T_{t1}$  to  $T_{t10}$ ) are used for validating the total flow force for  $\alpha = 2070$  and  $\beta = 1.2$ . In Fig. 9(c), the total horizontal force,  $F_x/F_B$ , is plotted against the incoming current velocity ( $U_t$ , or the towing velocity in experiments), where  $F_B$  is the buoyancy of fully submerged test model. Both measured and simulated results are provided for easy comparison. The error bars of measurement indicate the discrepancies among repeats. The predicted values follow the measurements closely with a slight underestimate (about 10%). The variation of  $F_x$  with  $U_t$  can be well described by a quadratic trend, i.e.,  $F_x = C_1 U_t + C_2 U_t^2$ , which suggests that the proposed form of porous drag force [Eq. (10)] is valid. To show some details of the simulation, we present the spanwise and horizontal middle-plane cuts of simulated 3D flow fields in Figs. 9(a) and 9(b). The water surface is piled up at the upstream edge of the porous structure, which is also observed in the experiments, while a 3D wake-like flow structure is predicted behind the structure. Since we do not have flow measurement, these results are just for illustration purposes.

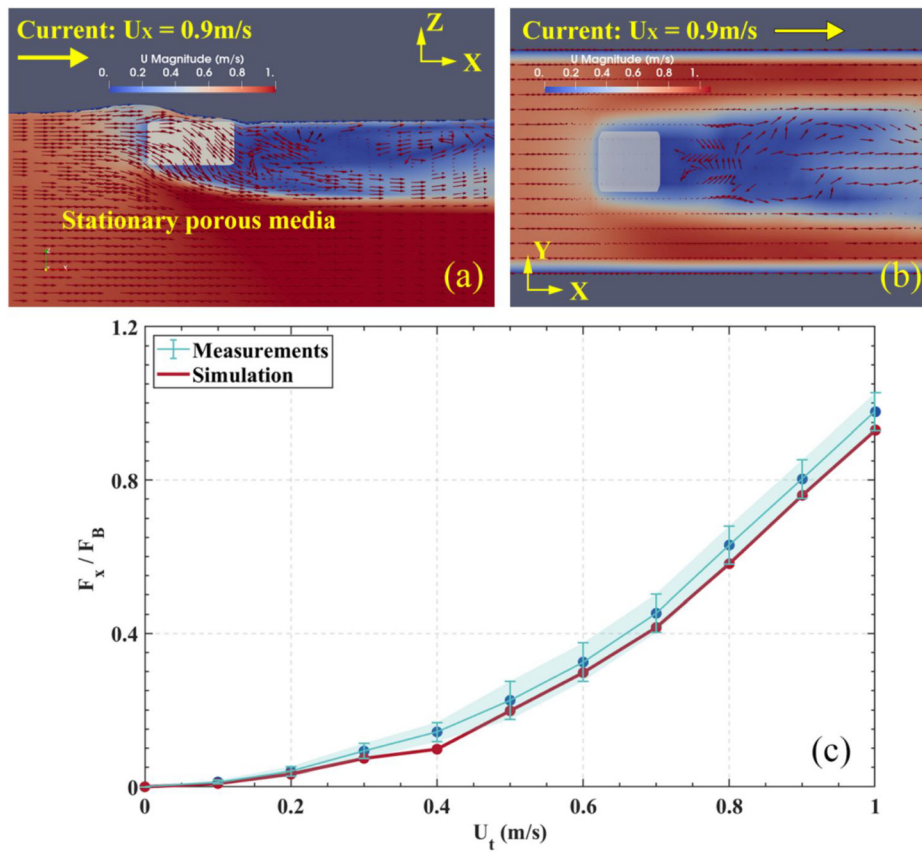
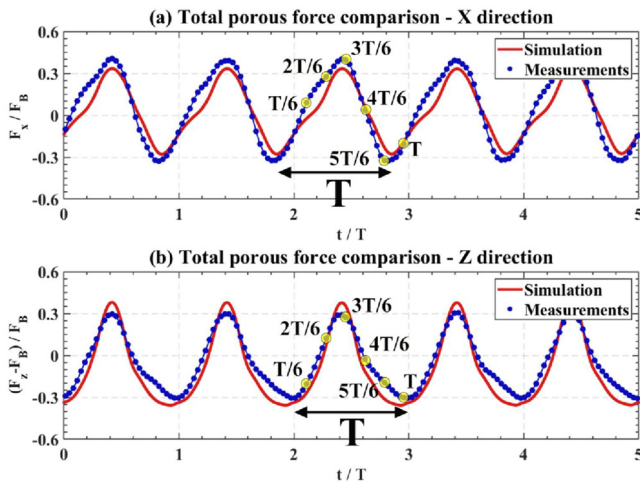


FIG. 9. Model validation for fixed porous structure in steady flow: (a) spanwise middle-plane cut of simulated flow field for test  $T_{t9}$ , (b) horizontal middle-plane cut of simulated flow field for test  $T_{t9}$ , and (c) measured and predicted total horizontal porous body forces as a function of towing velocity.



**FIG. 10.** Normalized total porous body force of 3D fixed porous structure test  $T_{w5}$ : (a) streamwise component  $F_x/F_B$  and (b) vertical component  $(F_z - F_B)/F_B$ . Only half of the measuring points are shown for clarity.

### C. Wave tests

Here, we first present a representative case, test  $T_{w5}$ . The normalized time series of predicted and measured force components,  $F_x/F_B$  and  $(F_z - F_B)/F_B$ , are presented in Fig. 10, where  $F_B$  is the buoyancy

of fully submerged test model. The relative error in predicting the magnitudes of  $F_x$  and  $F_z$  is about 10% (overestimate  $F_z$ , but underestimate  $F_x$ ). From the measurement, it can be seen that the time series of  $F_x$  is a bit forward-leaning and the time series of  $F_z - F_B$  has sharp crest and flat trough. These features were well captured by the numerical model. The measured maxima and minima of  $F_x$  and  $F_z$  occur at the same time, which is also suggested by the simulations.

To relate the total porous body force with the porous media flow, the spanwise cuts (following the model's streamwise centerline) of simulated porous body force field are presented in Fig. 11 for six representative time instances. Here  $t = 0$  is a rather arbitrary chosen instance when  $F_z - F_B$  is at its minimum. The maxima  $F_x$  and  $F_z$  occur around  $t = t_0 + T/2$  [Fig. 11(c)]. At this instance, the wave crest is about to arrive at the porous structure, which should give a strong forward fluid velocity, according to linear wave theory. The water free surface above the porous zone is also rising up, leading to an upward fluid velocity. Both velocity components are maximized around this instance, leading to the maxima of  $F_x$  and  $F_z$ . It can be seen that the porous force has a larger value at the edge of the porous body and decreases in the interior of the porous body due to the decrease in fluid velocity. At the phase  $t = t_0 + T$  [Fig. 11(f)], the wave trough is about to arrive at the porous zone and the local water surface is dropping rapidly, so the flow within the porous zone is mostly downward, leading to the minimum of  $F_z$ . Note that both measurements and simulations suggest that the minimum of  $F_x$  occurs slightly earlier than the minimum of  $F_z$ . This is because the strongest backward flow [at  $t = t_0 + 5/6T$ , see Fig. 11(e)] occurs a bit earlier than the strongest downward flow (at  $t = t_0 + T$ ).

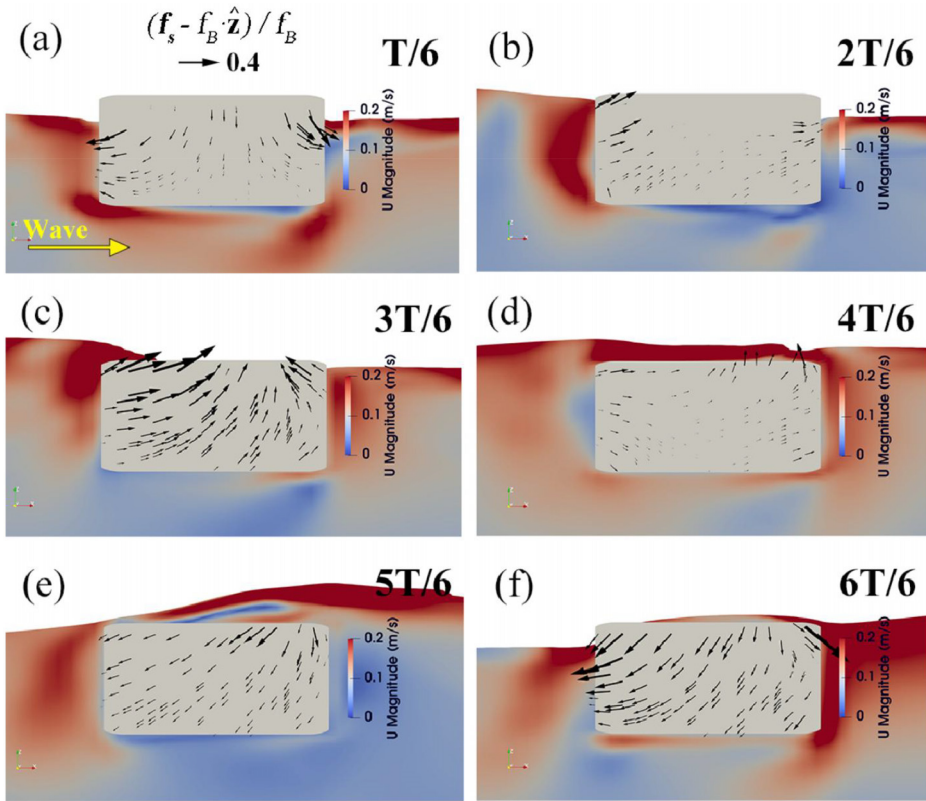


**FIG. 11.** Spanwise cut of simulated porous body force fields for six representative time instances of test  $T_{w5}$  [The arrows indicate  $(f_s - f_B \cdot \hat{z})/f_B$ , where  $f_s$  and  $f_B$  represents body force and buoyancy in each cell. The box outlined by the thin solid line indicates the fixed porous body. Wave travels from left to right. The timing of each snapshot is marked in Fig. 10: (a)  $t = t_0 + T/6$ , (b)  $t = t_0 + 2T/6$ , (c)  $t = t_0 + 3T/6$ , (d)  $t = t_0 + 4T/6$ , (e)  $t = t_0 + 5T/6$ , and (f)  $t = t_0 + 6T/6$ ].

In addition, it can be seen that the porous force is mainly distributed around the water surface.

Figure 12 shows the model-data comparison for the amplitude (defined as the maximum minus minimum) of body force for all wave tests ( $T_{w1}$  to  $T_{w6}$ ). The red points indicate total body force in  $z$  direction ( $F_z$ ), and the blue points indicate total body force in  $x$  direction ( $F_x$ ). When the point falls on the black solid line, the simulation and the measurements agree perfectly. The slope of least-square fit (the dashed lines) to the points indicate that the  $F_x$  is underestimated 11% and the  $F_z$  is overestimated 19% in simulations. The different model performance between  $F_x$  and  $F_z$  may suggest that the two force components do not share the same  $\alpha$  and  $\beta$  value. In other words, the porous media appears a bit anisotropic, despite that the structure's projections in  $x$  and  $z$  directions are the same. This may not be a surprising result. When a sphere is placed near the wall, it will experience a lift force perpendicular to the ambient wall-parallel flow, because the wall makes the flow around the sphere asymmetric. Here, the free water surface may act as a wall, so the total flow force is not in line with the flow velocity, and the parameter  $\beta$  is not longer isotropic. In the following work, we shall show that using the same value of  $\alpha$  and  $\beta$  still yields acceptable model performance, so we choose the same value of  $\alpha$  and  $\beta$  for  $F_x$  and  $F_z$ .

## V. MODEL APPLICATION: POROUS FLOATING STRUCTURES

In this section, the proposed numerical model is applied to simulate the wave-induced dynamic response of a porous structure consisting of uniform spheres. The setup of numerical simulation is first provided. Subsequently, model-data comparisons are discussed for the porous structure with and without mooring.

### A. Setup of numerical simulation

A two-dimensional computational mesh (see Fig. 13) was established for modeling the flume tests. The length of the domain was 8 m, and the height of the domain was 1.2 m. Model-B was placed with or without mooring in the numerical wave tank. The parameter settings

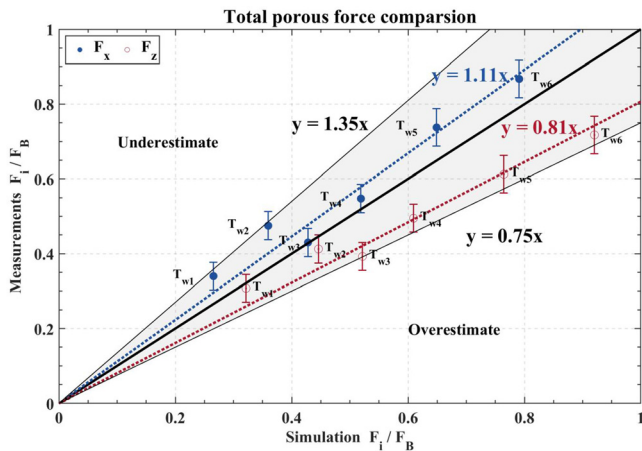


**FIG. 12.** Validation of total flow force using wave tests conditions ( $T_{w1}$  to  $T_{w6}$ ). The blue points and red points indicate total flow force in  $x$  and  $z$  direction ( $F_x$ ,  $F_z$ , respectively). The black solid line represents the best model-data agreement, while the dashed lines indicate the best fit to the data points.

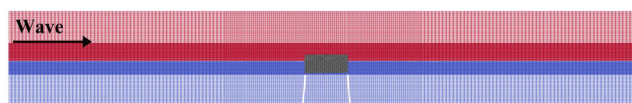


**FIG. 13.** An overview of the 2D computational domain and mesh. Wave is generated from the left side boundary (red region: air, blue region: water).

of mooring lines were kept consistent with the design in the experiment, i.e., the diameter of the mooring line was the volume-equivalent diameter in experiments, and the mass per unit length was also kept consistent with experiments (Hall, 2015). The axial stiffness ( $EA_0$ , where  $E$  is Young's modulus and  $A_0$  is the cross-sectional area of the mooring line) was set to 3000 N. The mesh was refined around the free surface and the porous structure. The total cell number was  $3.96 \times 10^4$ . The time step was set 0.01 s and will be adjusted according to the Courant number. The total simulation time was 50–80 s. A full simulation (covering 25–30 wave periods) can be finished within 0.5 h of

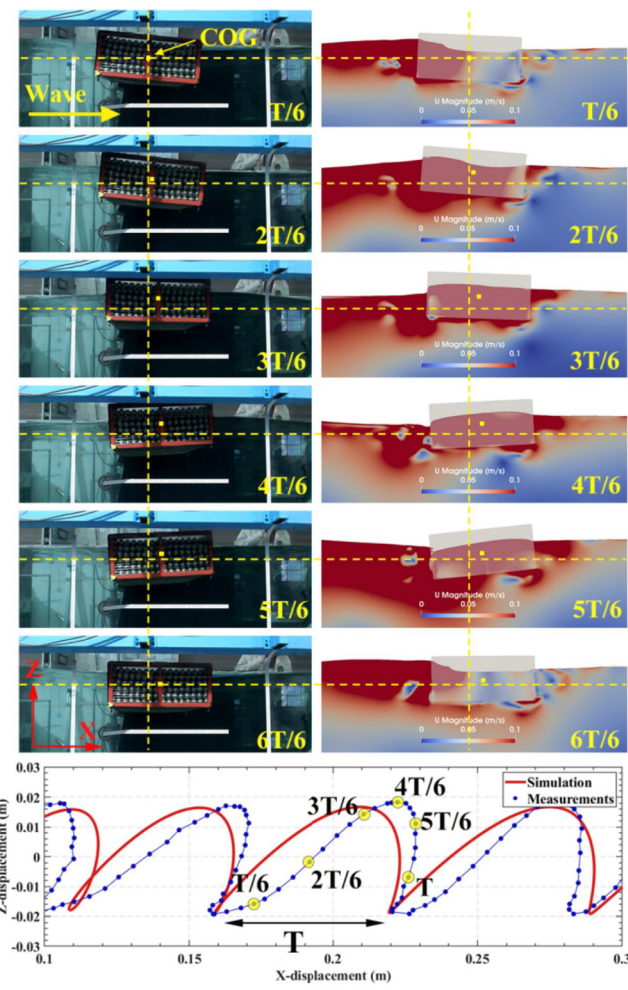


**FIG. 14.** Model-data comparison for free floating porous structure in waves (upper panels: screenshots for the predicted and measured response of the porous structure at six selected phases, lower panel: model-data comparison for the trajectory of CoG).

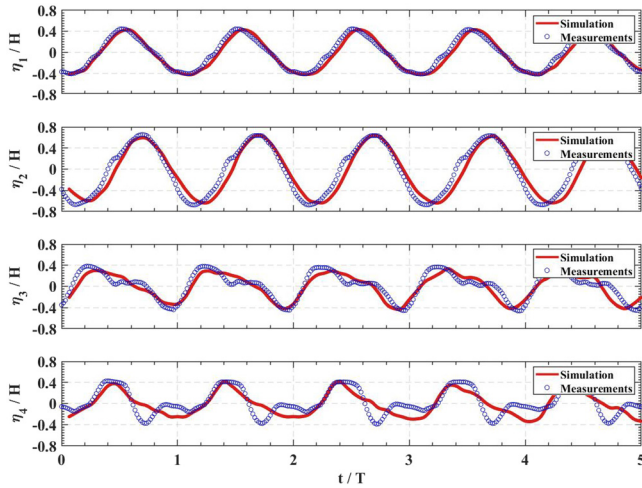


**FIG. 15.** Model-data comparison for the time history of the surface elevation of test  $T_{m4}$  at wave gauges WG1–WG4.

clocked time using Dell precision 7920 Tower with nine cores running in parallel, so the computational cost is moderate.

## B. Simulation of free-floating porous structures in waves

In test  $T_f$ , the porous structure freely floats on the water surface, which allows us to assess the CFD model's performance without the mooring model.

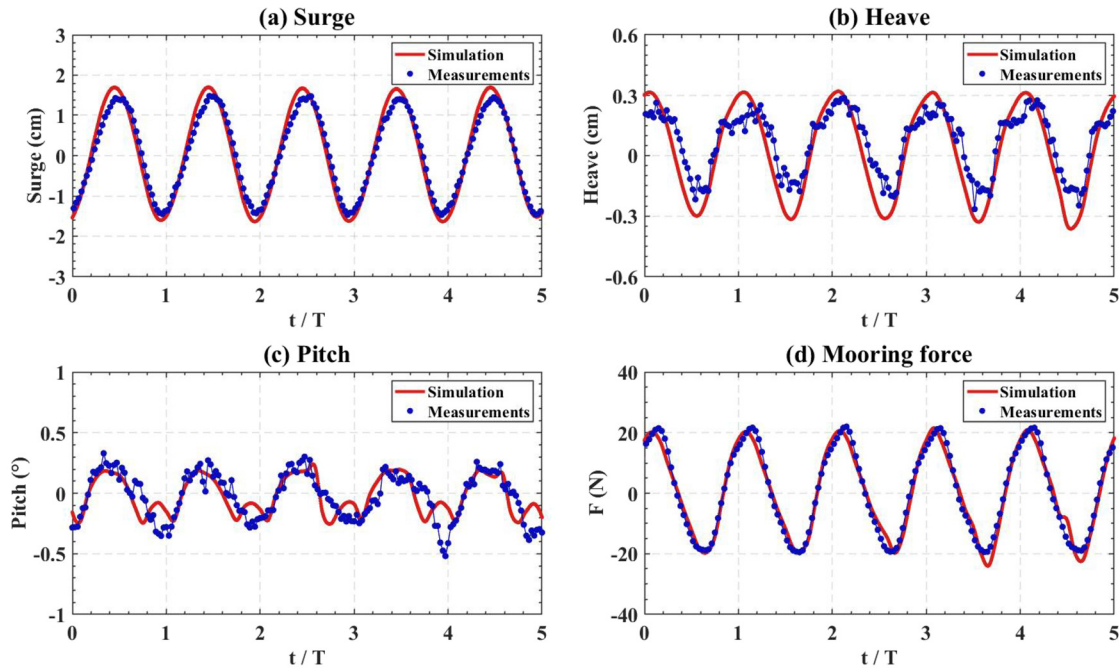


**FIG. 16.** Model-data comparison for 3DoF motion and fairlead mooring force: (a) surge, (b) heave, (c) pitch, and (d) mooring force at the fairlead of upstream mooring. Full circles are for the measurements, solid lines are for the model predictions. Only half of the measuring points are shown for clarity.

To show the dynamic response of the structure in waves, Fig. 14 side-by-side presents the snapshots from both video recordings and simulations for six phases ( $t/T = 1/6$  to  $6/6$ ). Here  $t=0$  is set at the instance when the wave crest is about to hit the structure. When the wave crest touches the upstream side of the porous structure ( $t/T = 1/6$ ), it begins to push the porous structure forward, and rotates the porous structure clockwise, i.e., rises the upstream side but lowers the downstream side. When the wave trough reaches the porous structure, it rotates the porous structure anticlockwise, but is unable to pull it backward ( $t/T = 3/6$  to  $5/6$ ). The simulated dynamic response of the porous structure follows the observation quite well. We marked the center of gravity (CoG) in each snapshot for showing the displacement of it. The lower panel of Fig. 14 compares the observed and simulated trajectories of CoG. There is a reasonable agreement between the two.

The free-floating porous structure drifted forward by about 0.06 m in one wave period, which is well predicted by the model. The excursion amplitude of the porous structure in the  $z$  direction is about 4 cm, which is also well predicted. There is a slight (about 5%–8%) variation of the  $x$ -direction excursion amplitude. Note that this simulation is limited in 12 periods, and the last three periods is shown in Fig. 14. As can be seen in Fig. 2, the mesh is deformed to accommodate the  $x$ -drift of the body, so the downstream-side mesh becomes increasingly finer than the upstream-side mesh as the body drifts downstream. The unbalanced mesh resolution makes the simulation of free-surface wave deteriorates period-by-period, until the mesh quality becomes bad enough to crash the simulation. This is the weakness of dynamic mesh method for large body displacement. Since the simulation within the last 3–6 periods are reasonably periodic, and is sufficient for model validation, we feel it is not necessary to further increasing the simulation

duration, which would require a much larger region for dynamic mesh if longer simulation. Note that there will not be a large  $x$ -drift for moored floating structure, so the simulation can cover as many periods as required.

Based on these model-data comparisons, it can be concluded that the rigid body motion of a free-floating porous structure in waves is modeled accurately. This demonstrates that the proposed approaches for calculating the porous body force and the 6DoF are valid.

### C. Simulation of the mooring-restrained porous structure in waves

#### 1. Simulation of test $T_{m4}$

In this subsection, the simulation of test  $T_{m4}$  is presented in detail to illustrate the model's fidelity. This test is the most representative one, because the porous structure had sufficient 6DoF, while wave attenuation was also apparent.

First, the model-data comparison for surface elevation,  $\eta$ , before and after the structure (i.e., at WG1 to WG4 in Fig. 5) is provided in Fig. 15. Here, the streamwise length of the computational domain is set as the same as the flume length (20 m), so the four wave gauges were all covered in the simulation.  $\eta$  is accurately predicted at WG1 and WG2, indicating that the incident and reflected waves are both well predicted by the model. At WG3 and WG4, the predicted  $\eta$  also shows a good agreement with the measurements. It is noted that a secondary peak of the surface elevation is present within one wave cycle, which suggests that the transmitted wave has a large second-harmonic component. For this test, the nonlinear quadratic porous body force leads to significant reduction of the leading first harmonic of  $\eta$ , while the nonlinearity (either from wave itself or the nonlinear body force) maintains a second harmonic, making the second harmonic appears significant. Therefore, the numerical simulation can adequately capture wave attenuation and associated nonlinear processes.

Second, the motion of the porous structure and the mooring force are validated, which allows us to evaluate the 6DoF and mooring modules defined in Fig. 3. Since the simulation is 2D, only three DoFs are involved, i.e., surge ( $x$  displacement), heave ( $z$  displacement) and pitch (rotation around the  $y$  axis). The model-data comparisons are shown in Fig. 16. The location of the CoG is obtained through recognizing the yellow markers in the video recordings, which is realized by averaging the coordinates of pixels with yellow colors. The reading error of CoG's coordinate is estimated to be about 0.5–1 pixels (or 0.3–0.7 mm). Due to the strong restrain of taut mooring, the heave of porous structure is only within  $\pm 2.5$  mm (or 3–4 pixels), so the relative reading error is larger than that for surge, making the time series wiggly. This is also the reason for the wiggly measurement of pitch. Nevertheless, the measurement error is still acceptable for validation. The 3DoF time series have rather sinusoidal shape. The surge and heave time histories are almost  $180^\circ$  out-of-phase, while the pitch and surge time histories are almost in-phase. These characteristics of time variation are well predicted. The worst model performance is for heave, which has an overestimate of about 15%. Both surge and pitch are predicted with an relative error of less than 10%. Here, the mooring force is evaluated at the fairlead of the upstream mooring line, and the mean mooring force is removed for better showing the time variation. The time

series of mooring force has a forward-leaning shape, and the maxima and minima are almost identical. The prediction very closely follows the measurement, so the adopt simple-yet-realistic mooring model is sufficiently accurate for our application.

To further demonstrate the fidelity of the proposed numerical model, the snapshots of animated simulation are compared to those from recorded video for six consecutive phases ( $t/T = 0$  to  $5/6$ ) in Fig. 17. The water surface in the recorded video is highlighted by yellow lines for easy identification. The main feature of water surface is the overwash process, i.e., the wave crest passes the top of porous structure (from  $T/3$  to  $5T/6$ ), which is accurately reproduced by the numerical simulation. The prediction also reveals that the flow velocity behind the porous structure is significantly lower than that before the porous structure, except for the free surface region where the overwash brings high velocity flow to the downstream side.

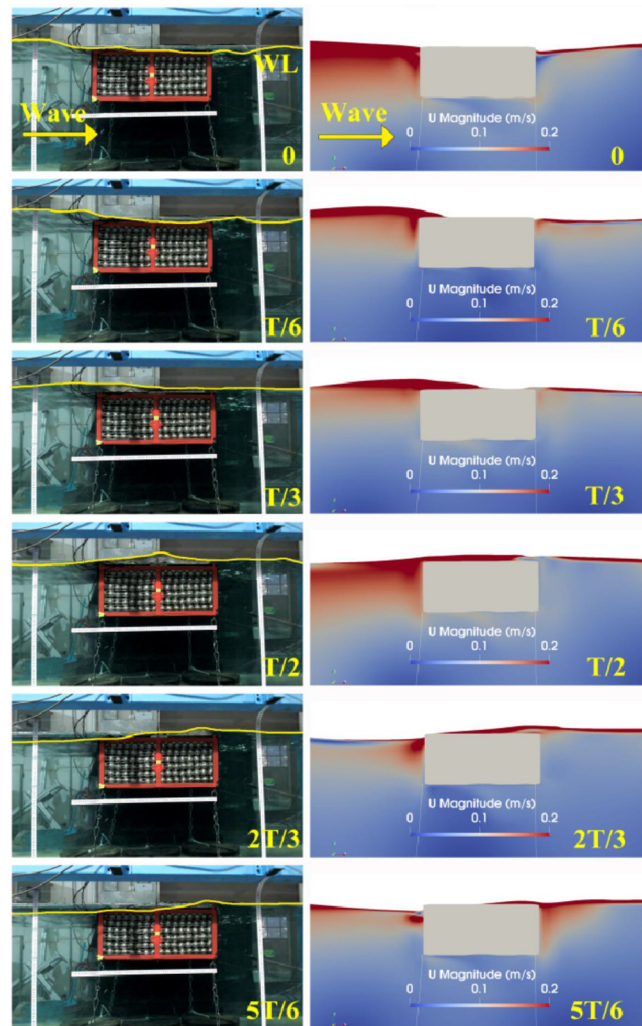


**FIG. 17.** Snapshots of animated simulation and recorded video at six selected phases for test  $T_{m4}$ . Left column is from recorded video of flume test, and the right column is the numerical simulation.

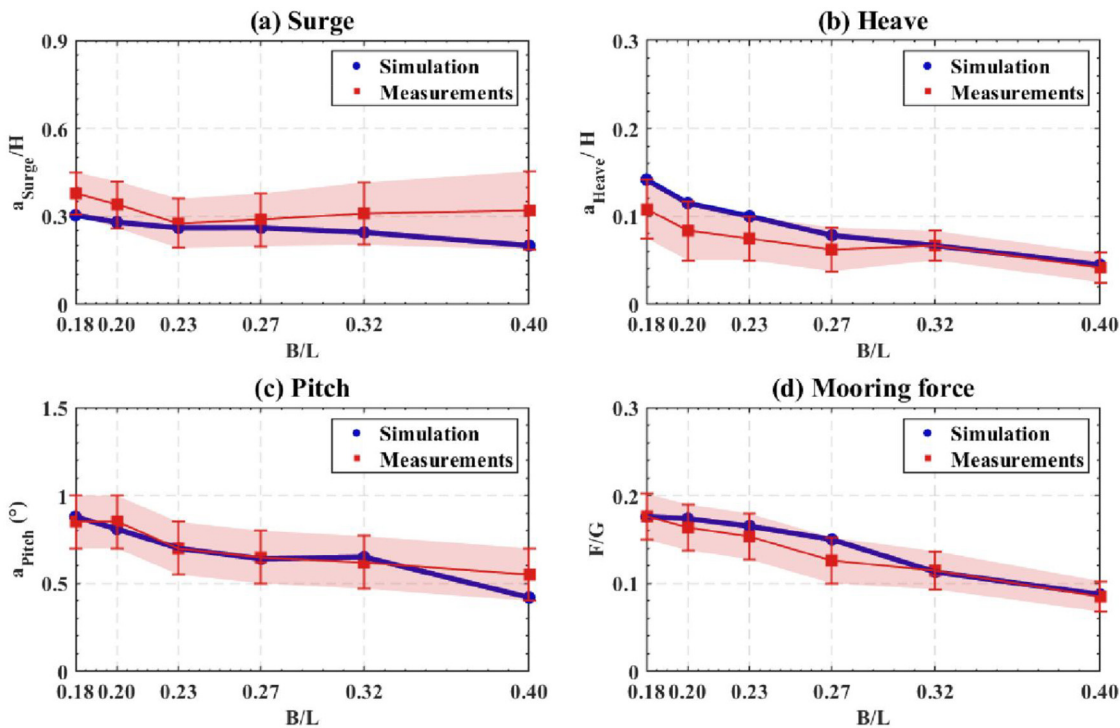


FIG. 18. Comprehensive model-data comparison of (a) surge, (b) heave, (c) pitch, and (d) mooring forces, for all the validation tests.

## 2. Overall model performance for moored porous structures in waves

It is of interest to evaluate the model's overall performance for tests with mooring. Here, we seek to demonstrate that the numerical model can reasonably capture the variations of 3DoF, mooring force, and wave transmission coefficient, with  $B/L$ . This will also demonstrate the capability of numerical simulations in aiding the design of porous structure.

Since the 3DoF and the mooring force are periodic, the model-data comparison is conducted based on the amplitude,  $a_{\xi}$ , defined as the average difference between maximum and minimum within a wave period, where  $\xi$  denotes the variable. The same as in Fig. 16, the mooring force at the fairlead of the upstream mooring line is considered. The results of  $a_{\xi}$  vs  $B/L$  are presented in Fig. 18. The error band of experimental results is given by the standard deviation of repeats. For all the four variables,  $a_{\xi}$  reduces with increasing  $B/L$ . This agrees with the common sense that shorter waves give smaller dynamic responses of a floating body and hence need smaller mooring restraints [e.g., Rahman *et al.* (2006); Christensen *et al.* (2018)]. The simulated results generally agree well with the measurements, and discrepancy is mostly less than the experimental error.  $a_{\text{surge}}$  is slightly underestimated, while  $a_{\text{heave}}$  is slightly overestimated, which agrees with model evaluation in Sec. IV C (i.e., in the porous drag force,  $x$  component is underestimated, while the  $z$  component is overestimated).

The transmission coefficient is defined as  $K_t = H_{tr}/H_{in}$ , where  $H_{tr}$  is the transmitted wave height and  $H_{in}$  is the incident wave height. Similarly, the reflection coefficient is defined as  $K_r = H_{re}/H_{in}$ , where

$H_{re}$  is the reflection wave height. Figure 19 presents the model-data comparison for  $K_t$  and  $K_r$  with varying  $B/L$ . It can be seen that  $K_t$  reduces with  $B/L$ , which agrees with the common understanding that floating breakwater can better block shorter waves. The model slightly

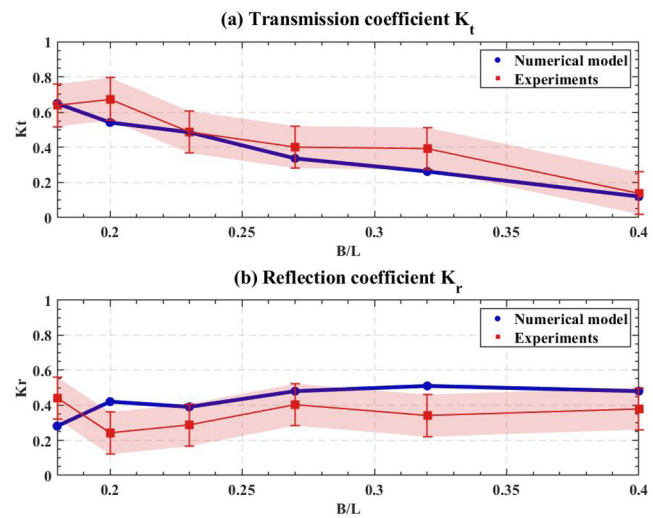


FIG. 19. Model-data comparison of  $K_t$  and  $K_r$  for varying  $B/L$ : (a) transmission coefficient  $K_t$  and (b) reflection coefficient  $K_r$ .

underestimates  $K_t$  by 5%–25% and overestimates  $K_r$  by 5%–25%. The discrepancy is comparable to the experimental error.

## VI. CONCLUSIONS

In the present study, a numerical approach is proposed for modeling porous floating structures in coastal flows. Here, the application is limited to rigid volumetric porous structures. The bulk effects of porous zone is treated as a volume averaged body force on the flow. The existing VARANS model is extended to floating porous media by using the relative velocity in the definition of porous friction force per unit volume. Following the convention of modeling bulk behavior porous media flow, the friction force is simply taken as the sum of a linear term and a quadratic term, which both have an empirical coefficient for model closure. The force and moment required for calculating 6DoF response is obtained by volume integrating the porous body force. The simulated 6DoF response is subsequently used to guide mesh deformation using the dynamic mesh method. Here the original dynamic mesh in OpenFOAM is modified by setting an inner zone, which covers the entire mesh in the porous body and moves according to the body's 6DoF response. A dynamic mooring model, Moody, is coupled to the flow solver for considering mooring restraints on the floating porous body. As a demonstration, the proposed numerical approach is applied to porous floating structures consisting of cubically packed uniform spheres. The two model parameters for the bulk friction force,  $\alpha$  and  $\beta$ , were obtained from other experimental study by Van Gent (1996).

First, the model is applied to three-dimensional flow around a fixed porous body. Flume tests were conducted using periodic waves to hit the structure or tow structure with a uniform speed in still water. The total body force in horizontal and vertical directions was measured and used for model validation. In towing test (steady flow condition), it was found that the model can yield predictions of streamwise total force with an inaccuracy of 10%. In wave tests (unsteady flow condition), it was found that  $F_x$  is underestimated 11% and  $F_z$  is overestimated 19% in simulations. This suggests that the two force components may not share the same empirical coefficients for drag force, which is possibly due to the anisotropy of the flow.

Second, the model is applied to two-dimensional wave-structure interaction for floating porous body representing a breakwater. For free-floating condition, the model can accurately predict the 3DoF of the structure, including the slow drift of it, and the comparison of animated simulation and recorded test videos show that the dynamic response of the porous structure in waves is depicted reasonably well by the model. For mooring-restrained conditions, here only taut mooring was studied. In addition to good predictions of 3DoF and porous structure's dynamic response, the mooring force is also predicted well. The numerical model also accurately depicts how porous structure's wave transmission coefficients reduce with the  $B/L$  parameter under the same wave height.

The numerical approach proposed in the present study can be applied to other coastal floating structures with a rigid volumetric porous body. The model parameters for friction force will surely change with different realization of the porous body and could be obtained through model calibrations using flume tests. For complex geometry of the porous structure or complex flow conditions, it is also necessary to further investigate the microscopic flow within the pores through either obtaining pore-flow measurements or conducting high-fidelity numerical simulations that directly resolve the pore flow.

Nevertheless, the macroscopic approach is computationally cheap enough for engineering applications, even for three-dimensional problems (e.g., short crested waves hitting a porous structure), so it is a valuable tool for coastal-engineering design. More future research is required to explore its applications in other scenarios, and to extend the model to flexible structures (e.g., floating vegetation patches).

## ACKNOWLEDGMENTS

This research is supported by the State Key Laboratory of Hydroscience and Engineering [Grant No. 2022-KY-05/(2022-KY-05)].

## AUTHOR DECLARATIONS

### Conflict of Interest

The authors have no conflicts to disclose.

### Author Contributions

**Yiyong Dong:** Data curation (equal); Formal analysis (equal); Methodology (equal); Software (equal); Writing—review & editing (equal). **Weikai Tan:** Methodology (equal); Software (equal); Writing—original draft (equal). **Hao Chen:** Supervision (equal); Writing—review & editing (equal). **Jing Yuan:** Conceptualization (equal); Methodology (equal); Project administration (equal); Supervision (equal); Writing—review & editing (equal).

## DATA AVAILABILITY

The data that support the findings of this study are available from the corresponding authors upon reasonable request.

## APPENDIX: CONVERGE STUDY

The mesh resolution deserves some further discussion. In our simulations, the porous zone is modeled with quite fine mesh. The grid size is one order of magnitude smaller than the diameter of sphere, which is the representative length scale of the pores. We first conducted a sensitivity analysis of grid size. Tests  $T_{w5}$  and  $T_{m4}$  were simulated using two more sets of mesh with finer and coarser

**TABLE V.** Sensitivity analysis of mesh resolution for tests  $T_{w5}$  and  $T_{m4}$ .

3D test $T_{w5}$	Low resolution	Medium resolution	High resolution
Cell number	−50%	...	+50%
$a_{F_x}$ (N)	25.1	26.8	28.1
$a_{F_z}$ (N)	28.5	30.0	31.6
2D test $T_{m4}$	Low resolution	Medium resolution	High resolution
Cell number	−50%	...	+50%
$a_{surge}$ (cm)	3.06	3.17	3.02
$a_{heave}$ (cm)	0.63	0.70	0.71
$a_{pitch}$ (°)	0.67	0.72	0.75
$a_{F_{mooring}}$ (N)	40	43	44

resolutions than the one used before, and the amplitudes of total body force ( $a_{F_x}$ ,  $a_{F_z}$ ), 3DoF ( $a_{\text{surge}}$ ,  $a_{\text{heave}}$ ,  $a_{\text{pitch}}$ ), and mooring forces ( $a_{F_{\text{mooring}}}$ ) are compared in Table V. For all the parameters listed herein, less than 10% variance is observed. Therefore, the adopted mesh resolution is sufficiently high to produce converged results.

## REFERENCES

- Chen, H. and Christensen, E. D., "Investigations on the porous resistance coefficients for fishing net structures," *J. Fluids Struct.* **65**, 76–107 (2016).
- Chen, H. and Christensen, E. D., "Development of a numerical model for fluid-structure interaction analysis of flow through and around an aquaculture net cage," *Ocean Eng.* **142**, 597–615 (2017).
- Chen, H. and Hall, M., "CFD simulation of floating body motion with mooring dynamics: Coupling MoorDyn with OpenFOAM," *Appl. Ocean Res.* **124**, 103210 (2022).
- Christensen, E. D., Bingham, H. B., Friis, A. P. S., Larsen, A. K., and Jensen, K. L., "An experimental and numerical study of floating breakwaters," *Coastal Eng.* **137**, 43–58 (2018).
- Chwang, A. and Chan, A., "Interaction between porous media and wave motion," *Annu. Rev. Fluid Mech.* **30**, 53–84 (1998).
- Dagan, G., *Flow and Transport in Porous Formations* (Springer Science & Business Media, 2012).
- Darcy, H., *Les fontaines publiques de Dijon* (Hachette Livre-BNF, 1856).
- del Jesus, M., Lara, J. L., and Losada, I. J., "Three-dimensional interaction of waves and porous coastal structures: Part I: Numerical model formulation," *Coastal Eng.* **64**, 57–72 (2012).
- Dong, G., Zheng, Y., Li, Y., Teng, B., Guan, C., and Lin, D., "Experiments on wave transmission coefficients of floating breakwaters," *Ocean Eng.* **35**, 931–938 (2008).
- Engelund, F., *On the Laminar and Turbulent Flows of Ground Water through Homogeneous Sand* (Akademiet for de Tekniske Videnskaber, 1953).
- Feichtner, A., Mackay, E., Tabor, G., Thies, P. R., and Johannig, L., "Comparison of macro-scale porosity implementations for CFD modelling of wave interaction with thin porous structures," *J. Mar. Sci. Eng.* **9**, 150 (2021).
- Forcheimer, P., "Wasserbewegung durch boden," *Z. Ver. Dtsch. Ing.* **45**, 1781–1788 (1901).
- Gu, Z. and Wang, H., "Gravity waves over porous bottoms," *Coastal Eng.* **15**, 497–524 (1991).
- Guo, Y., Mohapatra, S., and Soares, C. G., "Review of developments in porous membranes and net-type structures for breakwaters and fish cages," *Ocean Eng.* **200**, 107027 (2020a).
- Guo, Y., Mohapatra, S., and Soares, C. G., "Wave energy dissipation of a submerged horizontal flexible porous membrane under oblique wave interaction," *Appl. Ocean Res.* **94**, 101948 (2020b).
- Hall, M., "MoorDyn user's guide," Department of Mechanical Engineering, University of Maine, Orono, ME, 2015, p. 15.
- Han, M. and Wang, C., "Potential flow theory-based analytical and numerical modelling of porous and perforated breakwaters: A review," *Ocean Eng.* **249**, 110897 (2022).
- He, F., Huang, Z., and Wing-Keung Law, A., "Hydrodynamic performance of a rectangular floating breakwater with and without pneumatic chambers: An experimental study," *Ocean Eng.* **51**, 16–27 (2012).
- Higuera, P., "Application of computational fluid dynamics to wave action on structures," Ph.D. thesis, Universidad de Cantabria, Cantabria, Spain 2015.
- Higuera, P., Lara, J. L., and Losada, I. J., "Three-dimensional interaction of waves and porous coastal structures using OpenFOAM®. Part I: Formulation and validation," *Coastal Eng.* **83**, 243–258 (2014a).
- Higuera, P., Lara, J. L., and Losada, I. J., "Three-dimensional interaction of waves and porous coastal structures using OpenFOAM®. Part II: Application," *Coastal Eng.* **83**, 259–270 (2014b).
- Hirt, C. W. and Nichols, B. D., "Volume of fluid (VOF) method for the dynamics of free boundaries," *J. Comput. Phys.* **39**, 201–225 (1981).
- Hsu, T.-J., Sakakiyama, T., and Liu, P. L.-F., "A numerical model for wave motions and turbulence flows in front of a composite breakwater," *Coastal Eng.* **46**, 25–50 (2002).
- Ji, C. Y., Chen, X., Cui, J., Gaidai, O., and Incecik, A., "Experimental study on configuration optimization of floating breakwaters," *Ocean Eng.* **117**, 302–310 (2016).
- Jie, H., "Hydrodynamics of water waves interacting with breakwater or vegetation," Ph.D. thesis, National University of Singapore, Singapore, 2020.
- Koley, S., Vijay, K., Nishad, C., and Sundaravadivelu, R., "Performance of a submerged flexible membrane and a breakwater in the presence of a seawall," *Appl. Ocean Res.* **124**, 103203 (2022).
- Lara, J., Losada, I., and Guanche, R., "Wave interaction with low-mound breakwaters using a rans model," *Ocean Eng.* **35**, 1388–1400 (2008).
- Liu, P. L. F., Lin, P., Chang, K. A., and Sakakiyama, T., "Numerical modeling of wave interaction with porous structures," *J. Waterw., Port, Coastal Ocean Eng.* **125**, 322–330 (1999).
- Losada, I. J., Lara, J. L., Guanche, R., and Gonzalez-Ondina, J. M., "Numerical analysis of wave overtopping of rubble mound breakwaters," *Coastal Eng.* **55**, 47–62 (2008).
- Mansard, E. P. and Funke, E., "The measurement of incident and reflected spectra using a least squares method," in *Proceedings of International Conference on Coastal Engineering* (ASCE, 1980), pp. 154–172.
- Palm, J., "Mooring dynamics for wave energy applications," Ph.D. thesis, Chalmers Tekniska Hogskola, Gothenburg, Sweden, 2017.
- Palm, J., Eskilsson, C., and Bergdahl, L., "An hp-adaptive discontinuous Galerkin method for modelling snap loads in mooring cables," *Ocean Eng.* **144**, 266–276 (2017).
- Palm, J., Eskilsson, C., Paredes, G. M., and Bergdahl, L., "Coupled mooring analysis for floating wave energy converters using CFD: Formulation and validation," *Int. J. Mar. Energy* **16**, 83–99 (2016).
- Polubarnova-Kochina, P. Y., *Theory of Ground Water Movement* (Princeton University Press, 1952).
- Rahman, M. A., Mizutani, N., and Kawasaki, K., "Numerical modeling of dynamic responses and mooring forces of submerged floating breakwater," *Coastal Eng.* **53**, 799–815 (2006).
- Rose, H., "On the resistance coefficient–Reynolds number relationship for fluid flow through a bed of granular material," *Proc. Inst. Mech. Eng.* **153**, 154–168 (1945).
- Rusche, H., "Computational fluid dynamics of dispersed two-phase flow at high phase fractions," Ph.D. thesis, University of London, London, UK, 2002.
- Shih, R. S., "Experimental study on the performance characteristics of porous perpendicular pipe breakwaters," *Ocean Eng.* **50**, 53–62 (2012).
- Smith, G. M., "Comparison of stationary and oscillatory flow through porous media," Technical Report, Citeseer, 1991.
- Sollitt, C. K. and Cross, R. H., "Wave transmission through permeable breakwaters," in *Proceedings of International Conference on Coastal Engineering* (ASCE, 1972), pp. 1827–1846.
- Troch, P. and De Rouck, J., "Development of two-dimensional numerical wave flume for wave interaction with rubble mound breakwaters," in *Proceedings of International Conference on Coastal Engineering* (ASCE, 1998), pp. 1638–1649.
- Van Gent, M. R. A., "Formulae to describe porous flow," Communications on Hydraulic and Geotechnical Engineering, Report No. 1992-02, Delft University of Technology, 1992.
- Van Gent, M. R. A., "Wave interaction with permeable coastal structures," in *International Journal of Rock Mechanics and Mining Sciences and Geomechanics Abstracts* (Elsevier, 1996), p. 277A.
- Wang, H. and Sun, Z., "Experimental study of a porous floating breakwater," *Ocean Eng.* **37**, 520–527 (2010).
- Zhang, H., Sun, B., Li, Z., and Wang, F., "Wave attenuation and motion response of floating breakwater with sponge material," *Ocean Eng.* **277**, 114325 (2023).